Original Article

DOI: 10.5582/bst.2026.01026

The ATF5-GPER1 axis drives female protection in hepatocellular carcinoma through dual tumor-suppressive and immune-modulatory mechanisms

Zhiquan Xu[1,§], Hao Wang[1,§], Qiang He[1,§], Hongshuai Cui[2], Zhongjun Wu[1,*], Rui Liao[1,*]

[1] Department of Hepatobiliary Surgery, the First Affiliated Hospital of Chongqing Medical University, Chongqing, China;
[2] Department of Gastrointestinal Surgery, Qingdao Central Hospital, University of Health and Rehabilitation Sciences, Qingdao, China.

SUMMARY: Hepatocellular carcinoma (HCC) exhibits marked sexual dimorphism, with females demonstrating superior survival, yet the underlying molecular mechanisms remain unclear. We integrated bulk transcriptomics (GSE39791, TCGA-LIHC, GSE14520) and single-cell RNA sequencing (five datasets, $n = 58$ patients, 238,982 cells) with machine learning (LASSO, SVM, random forest) to identify female-protective genes driving HCC disparities. Activating transcription factor 5 (ATF5) emerged as a female-protective gene with higher expression in females versus males across cohorts. Single-cell analyses revealed ATF5 defines a female-enriched, low-grade malignant subcluster with elevated apoptotic programs and reduced proliferative signaling, and pseudotime analysis showed coordinated ATF5-GPER1 downregulation during malignant progression (Spearman $\rho = -0.52$ and -0.48; both $p < 0.001$). In the immune compartment, ATF5 marked a female-enriched IFN-γ^+ macrophage state with enhanced immunostimulatory programs and preferential CXCL9/10–CXCR3-mediated communication with CD8/NK cells. Mechanistically, ATF5 transcriptionally activates G protein-coupled estrogen receptor 1 (GPER1), forming an estrogen-responsive regulatory module that functionally suppresses proliferation, induces apoptosis (HepG2: 26.45% *vs*. 11.88%, $p < 0.0001$), and inhibits migration in a GPER1-dependent manner as demonstrated by rescue experiments. Tissue microarray validation ($n = 167$) confirmed high ATF5 expression predicts improved recurrence-free survival specifically in female patients (HR = 0.34, $p = 0.040$) but not males ($p = 0.080$). The ATF5-GPER1 axis represents a female-protective circuit operating through tumor-intrinsic suppression and immune remodeling, offering mechanistic insight into HCC sexual dimorphism and identifying ATF5 as a sex-specific prognostic biomarker with potential therapeutic implications.

Keywords: sex differences, transcription factor, estrogen signaling, tumor-associated macrophages, single-cell RNA sequencing

1. Introduction

Hepatocellular carcinoma (HCC) ranks as the sixth most common tumor globally and is the third leading cause of cancer-related mortality, accounting for 865,269 new cases and 757,948 deaths annually (*1*). A defining feature of HCC is its striking sexual dimorphism: men exhibit 2–3-fold higher incidence and consistently poorer survival compared to women (*2,3*). This robust pattern persists after adjusting for viral hepatitis, alcohol consumption, and metabolic factors, implicating intrinsic sex-based biological mechanisms (*4*).

Classical estrogen receptor pathways, particularly ERα, inhibit hepatocyte proliferation and suppress pro-inflammatory networks (*5,6*). However, clinical trials with estrogen-based interventions have failed (*7*), and accumulating evidence suggests canonical ER signaling alone cannot fully explain the sex disparity in HCC. This highlights a critical gap: unidentified sex-specific molecular circuits operating independently of classical estrogen-ER pathways.

Sex also profoundly influences the tumor immune microenvironment. Female HCC patients exhibit higher proportions of cytotoxic lymphocytes and M1-polarized macrophages, while male tumors are enriched for immunosuppressive myeloid populations (*8,9*). Female patients show more durable benefit from immune checkpoint inhibitors despite lower initial response rates (*10*), suggesting sex-specific immune architectures reshape therapeutic vulnerability. Yet the molecular determinants linking sex-biased gene expression to immune remodeling remain unexplored.

Single-cell RNA sequencing (scRNA-seq) has revolutionized understanding of tumor heterogeneity

(*11,12*), identifying sex-specific malignant cell states and immune vulnerabilities in lung cancer, melanoma, and bladder cancer (*13-15*). However, integrative single-cell analyses systematically interrogating sex differences in HCC at cellular resolution remain scarce.

Activating transcription factor 5 (ATF5), a member of the ATF/CREB transcription factor family, has been implicated in stress responses, differentiation, and survival (*16*). While exhibiting oncogenic functions in glioblastoma and breast cancer (*17*), its role in liver cancer and involvement in sex-biased HCC biology remain undefined. G protein-coupled estrogen receptor 1 (GPER1), a membrane-bound estrogen receptor mediating rapid non-genomic signaling (*18*), has emerged as a candidate mediator of estrogen's protective effects, yet its transcriptional regulation and contribution to HCC sexual dimorphism are unknown.

We employed an integrative approach combining bulk transcriptomics, single-cell RNA sequencing (five datasets, $n = 58$ patients, 238,982 cells), machine learning, and functional validation to identify molecular drivers of sexual dimorphism in HCC. We identified ATF5 as a female-biased tumor suppressor preferentially expressed in malignant hepatocytes and tumor-associated macrophages. ATF5 directly transactivates GPER1, establishing an estrogen-responsive circuit suppressing proliferation, inducing apoptosis, and inhibiting migration. Single-cell analyses revealed ATF5 delineates a female-enriched, low-grade malignant subcluster and an immunostimulatory IFN-γ^+ macrophage state with enhanced chemokine-mediated lymphocyte recruitment. Clinical validation ($n = 167$) confirmed high ATF5 predicts improved recurrence-free survival specifically in females. Our findings identify the ATF5-GPER1 axis as a novel female-protective circuit operating through dual tumor-intrinsic and immune-modulatory mechanisms.

2. Materials and Methods

2.1. Data acquisition and pprocessing

A retrospective HCC tissue microarray (TMA) was constructed from 167 patients who underwent curative hepatectomy at the First Affiliated Hospital of Chongqing Medical University (January 2020–January 2025). The study was approved by the institutional ethics committee (Approval No. 2024-607-01). Public bulk transcriptomic datasets were obtained from GEO (GSE39791, GSE14520) and TCGA-LIHC (GDC; 374 tumors and 59 adjacent tissues). Five GEO scRNA-seq datasets (GSE242898, GSE146115, GSE156625, GSE151530, GSE149614) were integrated, comprising 58 patients (14 females, 44 males) and 238,982 cells after quality control. Samples were categorized as female/male tumor (FC/MC) or adjacent tissue (FP/MP).

A retrospective HCC tissue microarray (TMA) was constructed from 167 patients who underwent curative hepatectomy at the First Affiliated Hospital of Chongqing Medical University (January 2020–January 2025). Of these, 140 patients (83.8%) were HBsAg-positive, reflecting the HBV-predominant etiology of HCC in this Chinese cohort. The study was approved by the institutional ethics committee (Approval No. 2024-607-01). Public bulk transcriptomic datasets were obtained from GEO (GSE39791, GSE14520) and TCGA-LIHC (GDC; 374 tumors and 59 adjacent tissues). Five GEO scRNA-seq datasets (GSE242898, GSE146115, GSE156625, GSE151530, GSE149614) were integrated, comprising 58 patients (14 females, 44 males) and 238,982 cells after quality control. Samples were categorized as female/male tumor (FC/MC) or adjacent tissue (FP/MP).

2.2. Transcriptomic and machine learning analyses

Differential expression analysis was conducted using limma (FDR < 0.05, $|\log_2 FC| > 0.58$). Feature selection was performed using LASSO, SVM, and random forest with 10-fold cross-validation, and pathway enrichment was evaluated by GSEA. Prognostic analyses used Kaplan–Meier (log-rank) and Cox regression. Diagnostic performance was assessed by ROC analysis (AUC with DeLong confidence intervals).

2.3. Single-cell RNA-seq data processing

scRNA-seq data were processed in Seurat with standard quality control, normalization, integration, clustering, and UMAP visualization, followed by cell-type annotation using canonical markers. Malignant cells were inferred by inferCNV using immune/stromal cells as references and a conservative CNV-score threshold (0.0321), yielding 38,844 malignant cells. Macrophages (23,093 cells) were re-clustered and annotated into functional subtypes, including IFN-γ^+ macrophages defined by interferon-stimulated gene expression. Pseudotime trajectories were reconstructed using Monocle3 (Cluster 3 as the root), cell–cell communication was analyzed using CellChat, and bulk immune infiltration in TCGA-LIHC was estimated by ssGSEA with Bindea immune signatures.

2.4. Multiplex immunofluorescence and quantification

FFPE TMA sections (4 μm) were subjected to antigen retrieval (Tris–EDTA, pH 9.0) and sequential multiplex immunofluorescence using primary antibodies against ATF5 (Cell Signaling Technology #94850), CD68 (Abcam ab125212), and GPER1 (Abcam ab39742), followed by microwave-based stripping between cycles and DAPI counterstaining. Slides were scanned on a Vectra Polaris system and quantified with QuPath. Mean fluorescence intensity per core was background-corrected and normalized; survival analyses used median cutoffs and Cox regression.

2.5. Transcription factor binding site prediction

ATF5 motif analysis was performed using JASPAR (MA0833.1). The GPER1 promoter region (−2 kb from TSS; hg38) was retrieved from UCSC, and binding sites were predicted using FIMO ($p < 1\times10^{-4}$). To explore the mechanistic basis of female-biased ATF5 expression, the ATF5 promoter region (chr19:49,926,906–49,928,906, GRCh38) was scanned for estrogen response elements (EREs) using FIMO with JASPAR position weight matrices for ESR1 (MA0112.3, $p < 1\times10^{-4}$) and ESR2 (MA0258.1, $p < 0.001$). DNA methylation at ATF5 promoter CpG probes (HM450 array) was retrieved from TCGA-LIHC and compared between sexes using Wilcoxon tests; Spearman correlation was used to assess the relationship between promoter methylation (mean β value) and ATF5 mRNA expression.

2.6. Cell culture and hhormone treatments

HepG2 (CL-0103) and Huh7 (CL-0120) cells (Procell, Wuhan, China) were maintained in DMEM with 10% FBS and antibiotics at 37°C with 5% CO_2 and authenticated by STR profiling. For hormone stimulation, cells were conditioned in phenol red–free medium with charcoal-stripped FBS and treated with E2 (10 nM), G-1 (100 nM), and/or G36 (10 μM) for 24 h, with G36 added 1 h before E2 where indicated.

2.7. Gene manipulation

ATF5 knockdown was achieved using lentiviral shRNA with puromycin selection. ATF5 overexpression used pcDNA3.1-based transfection, and GPER1 knockdown used siRNA transfection. Perturbation efficiency was validated by qRT-PCR and Western blotting.

2.8. Molecular assays

qRT-PCR was performed using standard TRIzol-based RNA extraction, reverse transcription, and SYBR-based quantification with β-actin normalization ($2^{-\Delta\Delta Ct}$). Western blotting was performed using RIPA lysates, SDS-PAGE, PVDF transfer, immunodetection, and ImageJ quantification. Dual-luciferase assays were conducted using WT/MUT GPER1 promoter reporters co-transfected with ATF5 and Renilla control, and measured at 48 h.

2.9. Functional assays

Cell proliferation was assessed by CCK-8. Apoptosis was quantified by Annexin V/7-AAD flow cytometry. Migration was evaluated by wound-healing assays with image-based quantification.

2.10. Macrophage–T ccell co-culture assay

PMA-differentiated THP-1 macrophages were transduced with lentiviral shATF5 or shNC constructs and selected with puromycin. Conditioned medium was collected after 24 h serum-free culture and filtered (0.22 μm). Peripheral blood-derived $CD8^+$ T cells were stimulated with anti-CD3/CD28 beads and cultured in conditioned medium (1:1 ratio) for 48 h. CXCL9 and CXCL10 concentrations in conditioned medium were quantified by ELISA (R&D Systems). $CD8^+$ T cell activation was assessed by flow cytometry using anti-CD8 and anti-CD69 antibodies, with $CD8^+CD69^+$ frequency reported as the activation index.

2.11. Statistical analysis

Analyses were performed in R or GraphPad Prism. Two-group comparisons used Welch's *t*-test or Wilcoxon tests; multi-group comparisons used ANOVA or Kruskal–Wallis tests with appropriate post hoc corrections. Correlations used Spearman tests. Survival analyses used Kaplan–Meier and Cox regression. A multivariable nomogram for predicting 1- and 3-year recurrence-free survival was constructed using the rms package in R, incorporating ATF5 expression, sex, BCLC stage, age, and AFP as covariates based on a Cox proportional hazards model; model discrimination was assessed by Harrell's C-index and time-dependent AUC using the timeROC package, with calibration evaluated by bootstrap resampling (B = 200). Incremental predictive value of ATF5 was assessed by comparing the full model versus a base clinical model (BCLC stage, age, AFP, and sex) using time-dependent AUC at 1- and 3-year timepoints. Two-sided $p < 0.05$ was considered significant, and all cell-based experiments included ≥ 3 independent biological replicates.

3. Results

3.1. Integrative transcriptomic and machine learning analyses identify ATF5 as a female-protective ggene

To systematically identify molecular drivers of sexual dimorphism in HCC, we performed differential expression analysis on GSE39791 (72 samples: 58 males, 14 females). Comparing tumor versus adjacent tissues identified 4,235 differentially expressed genes (DEGs), while female versus male tumors revealed 196 sex-associated DEGs, with 100 genes overlapping both comparisons (Figure 1A-B). Directionally consistent filtering yielded 29 candidates: 4 female-protective (P>C and FC>MC) and 25 male-risk (C>P and MC>FC) genes, enriched for antigen processing pathways (adjusted $p < 0.05$; Figure 1C-D).

Three machine learning algorithms (LASSO, SVM, random forest) with 10-fold cross-validation identified nine consensus genes for tumor discrimination and six for sex stratification. Only ATF5 and WDR72 were

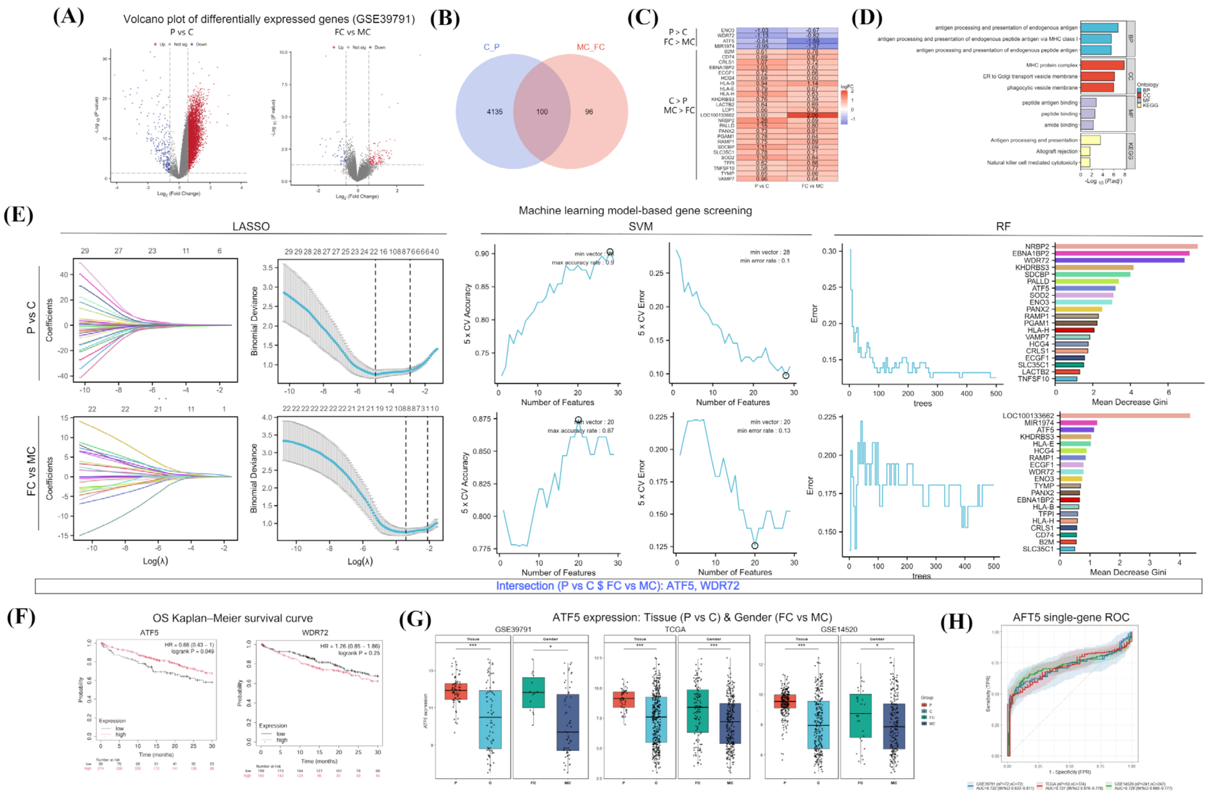

Figure 1. Integrated bulk transcriptomics and machine learning identify ATF5 as a female-protective candidate in hepatocellular carcinoma (HCC). (A) Volcano plots of differentially expressed genes (DEGs) in GSE39791 for tumor versus adjacent non-tumor tissues (C *vs*. P) and female versus male tumors (FC *vs*. MC). Significant DEGs are highlighted ($|\log_2FC| > 0.58$, false discovery rate [FDR] < 0.05). **(B)** Venn diagram showing overlap between tumor-associated DEGs (C *vs*. P) and sex-associated DEGs (FC *vs*. MC). **(C)** Directionally consistent filtering of shared genes to define female-protective (P > C and FC > MC) and male-risk (C > P and MC > FC) patterns; heatmap shows $\log_2$ fold changes. **(D)** Gene Ontology (GO) and Kyoto Encyclopedia of Genes and Genomes (KEGG) enrichment analysis of candidate genes. **(E)** Feature selection using least absolute shrinkage and selection operator (LASSO), support vector machine (SVM), and random forest (RF) with 10-fold cross-validation for C *vs*. P and FC *vs*. MC tasks; shared features are indicated. **(F)** Kaplan–Meier overall survival in The Cancer Genome Atlas Liver Hepatocellular Carcinoma cohort (TCGA-LIHC) stratified by median gene expression (ATF5 and comparator gene shown). **(G)** ATF5 expression validation across independent datasets (GSE39791, TCGA-LIHC, GSE14520) by tissue status and sex. **(H)** Receiver operating characteristic (ROC) curves and area under the curve (AUC) for ATF5 discriminating tumor versus adjacent tissue across datasets (AUC with 95% confidence interval shown). Statistical significance is denoted as: ns, not significant; *$p < 0.05$; **$p < 0.01$; ***$p < 0.001$; ****$p < 0.0001$.

shared across both tasks (Figure 1E). Kaplan-Meier analysis in TCGA-LIHC showed ATF5 associated with improved overall survival (median: high 65.2 *vs*. low 42.8 months; log-rank $p = 0.048$), whereas WDR72 lacked prognostic value ($p = 0.25$; Figure 1F).

ATF5 consistently showed higher expression in adjacent versus tumor tissues and in female versus male tumors across three independent datasets (GSE39791, TCGA-LIHC, GSE14520; all $p < 0.01$; Figure 1G). ROC analysis demonstrated reproducible diagnostic performance (AUC: GSE39791 0.89 [95% CI: 0.82–0.96], TCGA-LIHC 0.76 [0.71–0.81], GSE14520 0.71 [0.64–0.78]; Figure 1H).

3.2. Single-cell transcriptomic atlas confirms female-biased ATF5 expression in malignant hepatocytes

Integration of five scRNA-seq datasets (GSE242898, GSE146115, GSE156625, GSE151530, GSE149614; 58 patients, 238,982 cells) with Harmony batch correction yielded 23 clusters annotated into epithelial/hepatocyte-lineage, immune, and stromal populations (Supplementary Figure S1A, *https://www.biosciencetrends.com/action/getSupplementalData.php?ID=290*, Figure 2A-B). inferCNV analysis using epithelial-lineage cells (n = 59,071) as observation and immune/stromal cells (n = 49,154) as reference classified 38,844 malignant cells based on CNV score threshold (95th percentile = 0.0321), comprising 65.2% hepatocyte-like and 31.1% epithelial-like cells (Figure 2C-D).

ATF5 expression concentrated in epithelial/hepatocyte-lineage cells and macrophages (Figure 2E). Within malignant cells, ATF5 showed female bias: mean expression FC 0.26 versus MC 0.21 (Wilcoxon $p < 0.01$); ATF5-positive fraction FC 17.5% versus MC 12.4% (chi-square $p < 0.001$; Figure 2F).

Multiplex immunofluorescence on independent tissue microarray (n = 167: FC 27, MC 140, FP 26, MP 133) confirmed female-biased ATF5 protein expression (Figure 2G). Quantification showed significantly

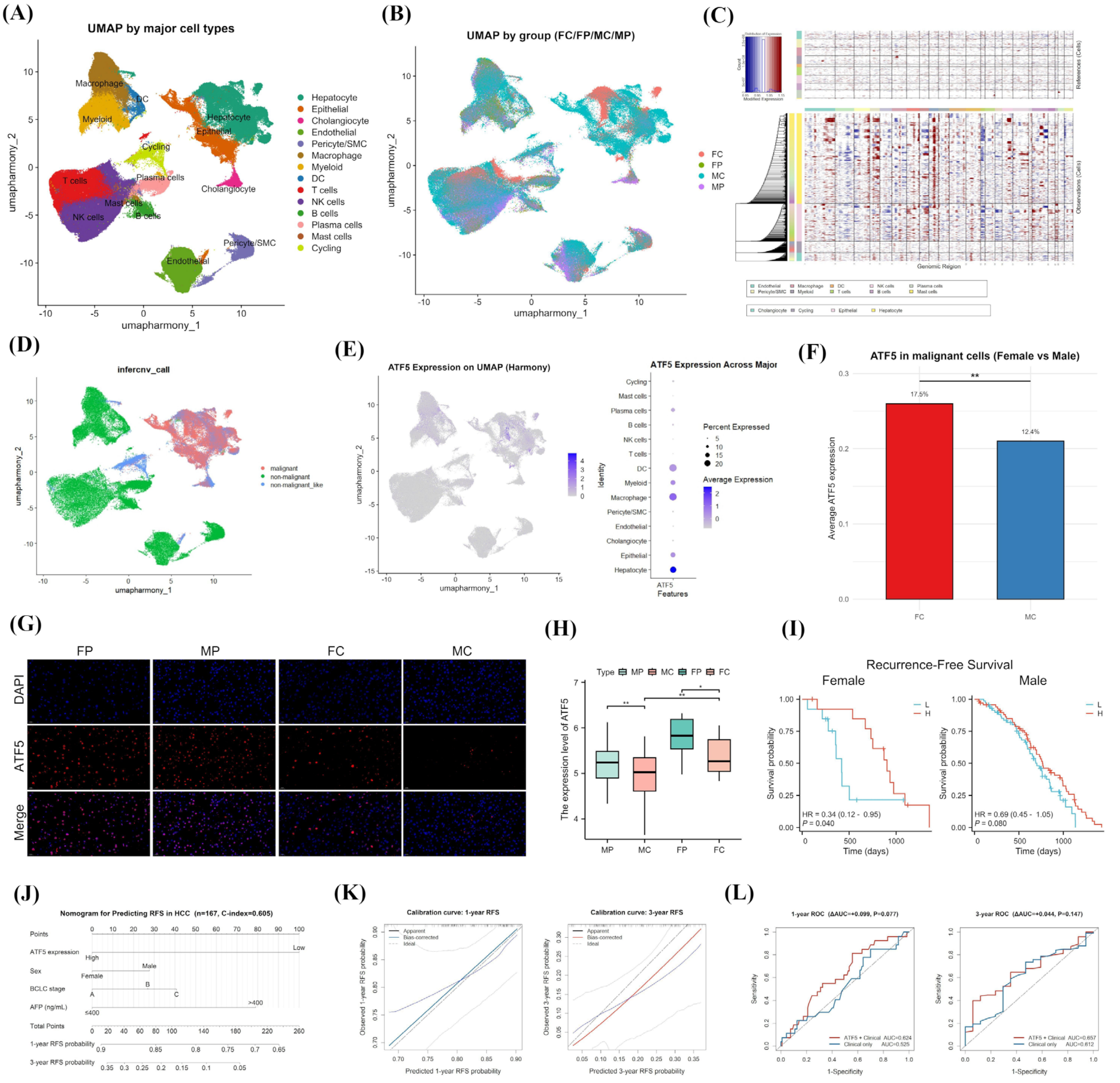

Figure 2. Single-cell and tissue-level validation confirms female-biased ATF5 expression in malignant cells and association with recurrence-free survival. (A) Uniform manifold approximation and projection (UMAP) of the integrated single-cell RNA-seq (scRNA-seq) atlas from five GEO datasets, colored by annotated major cell types. **(B)** UMAP colored by clinical group (FC/FP/MC/MP), illustrating Harmony-based integration. **(C)** inferCNV heatmap showing copy-number variation (CNV) profiles in reference (immune/stromal) and observation (epithelial-lineage) cells. **(D)** UMAP showing inferCNV-based malignancy classification using a reference-derived CNV-score threshold (malignant *vs*. non-malignant-like). **(E)** ATF5 expression in the atlas (feature plot) and across major cell types (dot plot). **(F)** Sex-stratified ATF5 expression and ATF5-positive cell fraction in malignant cells (tests indicated in the panel). **(G)** Representative multiplex immunofluorescence (mIF) images of ATF5 with 4′,6-diamidino-2-phenylindole (DAPI) across FP/MP/FC/MC groups (scale bar shown). **(H)** Quantification of ATF5 fluorescence intensity across groups (global and pairwise comparisons indicated in the panel). **(I)** Sex-stratified Kaplan–Meier recurrence-free survival (RFS) in the tissue microarray (TMA) cohort using median ATF5 as cutoff; hazard ratio (HR) and log-rank P are shown. **(J)** Nomogram integrating ATF5 expression, sex, BCLC stage, and AFP (ng/mL) for predicting 1- and 3-year RFS probability in the TMA cohort (*n* = 167, C-index = 0.605). **(K)** Calibration curves for the nomogram-predicted 1-year (left) and 3-year (right) RFS probabilities; the black line indicates apparent performance, the colored line indicates bias-corrected performance (bootstrap, B = 200), and the dashed line represents ideal calibration. **(L)** Time-dependent ROC curves comparing the full model (ATF5 + clinical variables) versus the base clinical model at 1-year (left) and 3-year (right) timepoints; AUC values and ΔAUC are shown.

higher ATF5 in FC versus MC (Dunn's $p = 0.001$) and FP versus MP ($p = 0.020$; Figure 2H). Sex-stratified survival analysis revealed high ATF5 predicted improved recurrence-free survival in females (median 48.2 *vs*. 28.6 months; HR = 0.34, 95% CI 0.12–0.95, $p = 0.040$) but not males (36.4 *vs*. 28.9 months; HR = 0.69, $p = 0.080$; Figure 2I).

To further evaluate the clinical utility of ATF5, we constructed a nomogram integrating ATF5 expression, sex, BCLC stage, and AFP to predict RFS in the TMA cohort (Figure 2J). The nomogram achieved a C-index of 0.605, and calibration curves demonstrated good agreement between predicted and observed RFS probabilities at both 1- and 3-year timepoints (Figure 2K). Time-dependent ROC analysis showed that incorporating ATF5 into the clinical model improved the AUC at 1-year (0.624 *vs*. 0.525, ΔAUC = +0.099) and 3-year (0.657 *vs*. 0.612, ΔAUC = +0.044) timepoints compared to the base model. Although statistical significance was not reached, likely due to the limited sample size of this single-center cohort ($n = 167$), the consistent AUC improvement across both timepoints supports the incremental prognostic contribution of ATF5 beyond conventional clinical staging (Figure 2L).

3.3. ATF5 ddelineates an IFN-γ^+ macrophage subset with enhanced immunostimulatory programs

Macrophage reclustering ($n = 23{,}093$, resolution 0.6) identified 16 subclusters including IFN-γ^+ macrophages characterized by interferon-stimulated genes (ISG15, IFIT1, IFIT2, MX1, OAS1, STAT1), which showed highest ATF5 expression (Figure 3A-B, Supplementary Figure S2A-B, *https://www.biosciencetrends.com/action/getSupplementalData.php?ID=290*). Among 53 patients with sufficient macrophages (12 females, 41 males), females showed significantly higher ATF5-high cell proportions within IFN-γ^+ macrophages (median 28.4% *vs*. 18.7%; Wilcoxon $p < 0.05$; Figure 3C).

Differential expression analysis identified 319 upregulated and 149 downregulated genes in ATF5-high versus ATF5-low IFN-γ^+ macrophages ($|\log FC| \geq 0.25$, FDR < 0.05; Figure 3D). AUCell scoring revealed ATF5-high cells exhibited higher activity in antigen presentation (median AUC 0.52 *vs*. 0.38; $p < 0.001$), IFN response (0.61 *vs*. 0.42; $p < 0.001$), inflammatory response (0.58 *vs*. 0.44; $p < 0.001$), phagocytosis (0.48 *vs*. 0.39; $p < 0.01$), and cytotoxicity (0.44 *vs*. 0.32; $p < 0.01$), but lower immunosuppression (0.28 *vs*. 0.41; $p < 0.001$) and lipid metabolism (0.31 *vs*. 0.46; $p < 0.001$) scores (Figure 3E).

CellChat analysis revealed ATF5-high IFN-γ^+ macrophages preferentially engaged CD8/NK cells *via* CXCL9/10–CXCR3 (interaction strength 0.42 *vs*. 0.08; $p < 0.01$) and CCL5–CCR5 (0.36 *vs*. 0.12; $p < 0.01$), whereas ATF5-low cells showed stronger TGFB–TGFBR (0.38 *vs*. 0.15; $p < 0.01$) and SPP1–CD44 (0.41 *vs*. 0.18; $p < 0.01$) interactions (Figure 3F, Supplementary Figure S2C, *https://www.biosciencetrends.com/action/getSupplementalData.php?ID=290*).

In TCGA-LIHC ($n = 374$), ATF5-high tumors showed elevated macrophage scores (median 0.58 *vs*. 0.42; $p < 0.01$; Figure 3G). An IFN-γ^+ macrophage signature score constructed from top 30 marker genes was higher in ATF5-high females (0.52 *vs*. 0.36; $p < 0.01$) but not males (0.42 *vs*. 0.38; $p = 0.12$; Figure 3H). Tissue microarray validation confirmed higher ATF5$^+$CD68$^+$ proportions in FC versus MC tumors (2.8% *vs*. 1.6%; Wilcoxon $p < 0.05$; Figure 3I-J).

To functionally validate these findings, we knocked down ATF5 in PMA-differentiated THP-1 macrophages (Figure 3K). ELISA showed that ATF5 knockdown significantly reduced CXCL9 (118.4 ± 14.5 *vs*. 309.2 ± 44.9 pg/mL; $p < 0.01$) and CXCL10 (164.9 ± 18.3 *vs*. 401.4 ± 45.9 pg/mL; $p < 0.01$) secretion (Figure 3L). Conditioned medium from shATF5 macrophages markedly attenuated CD8$^+$ T cell activation (CD8$^+$CD69$^+$: 6.74 ± 0.77% *vs*. 25.47 ± 1.65%; $p < 0.001$; Figure 3M), confirming a causal role of ATF5 in macrophage-mediated CD8$^+$ T cell recruitment *via* the CXCL9/10–CXCR3 axis.

3.4. ATF5 directly transactivates GPER1 through an estrogen-responsive circuit

Gene Set Enrichment Analysis on ATF5-stratified GSE39791 tumors revealed significant enrichment of estrogen-related pathways in ATF5-high tumors (all NES > 1.5, FDR < 0.05), including Reactome Estrogen Dependent Gene Expression (NES = 1.652), WikiPathway Estrogen Metabolism (NES = 1.909), WikiPathway Estrogen Receptor Pathway (NES = 1.929), and WikiPathway Estrogen Signaling Pathway (NES = 1.654; Figure 4A).

Spearman correlation analysis identified GPER1 as most strongly associated with ATF5 ($\rho = 0.356, p < 0.001$) compared to ESR1 ($\rho = 0.209$, $p = 0.012$) and ESR2 ($\rho = 0.289$, $p < 0.001$; Figure 4B), reproducible across TCGA-LIHC ($\rho=0.078$, $p < 0.001$) and GSE14520 ($\rho = 0.339$, $p < 0.001$; Figure 4C). Single-cell patient-level pseudobulk analysis confirmed ATF5-GPER1 correlation ($\rho = 0.345$, $p = 0.040$; Figure 4D). ATF5-high malignant cells showed markedly elevated GPER1 (median 0.045 *vs*. 0.021; Wilcoxon $p = 2.24 \times 10^{-29}$), more pronounced in females (Figure 4E).

JASPAR motif analysis identified ATF5 binding sites in GPER1 promoter (−2kb to +200bp; FIMO $p < 1\times10^{-4}$; Figure 4F, Supplementary Figure S3A, *https://www.biosciencetrends.com/action/getSupplementalData.php?ID=290*). Lentiviral shRNA-mediated ATF5 knockdown reduced GPER1 protein concomitantly with ATF5 depletion (HepG2: ATF5 to 32% of control, $p = 0.003$; GPER1 to 38%, $p = 0.001$; Huh7: ATF5 to 28%, $p = 0.004$; GPER1 to 35%, $p = 0.001$; $n = 3$; Figure 4G). Dual-luciferase assays showed ATF5 increased wild-type GPER1 promoter activity 3.14-fold ($p = 5.35 \times 10^{-5}$) but not mutant promoter ($p = 0.277$; Figure 4H).

Hormone treatments (E2 10nM, G-1 100nM) upregulated ATF5 (E2: 1.82-fold, $p < 0.01$; G-1: 1.64-fold, $p < 0.05$) and GPER1 mRNA (E2: 2.15-fold, $p < 0.01$; G-1: 1.88-fold, $p < 0.05$), while GPER1 antagonist G36 (10μM) blocked E2-induced upregulation (both $p < 0.05$; Figure 4I, Supplementary Figure S3B, *https://www.biosciencetrends.com/action/getSupplementalData.php?ID=290*). Western blot confirmed protein-level regulation (E2: ATF5 1.76-fold, $p < 0.05$; GPER1 2.08-

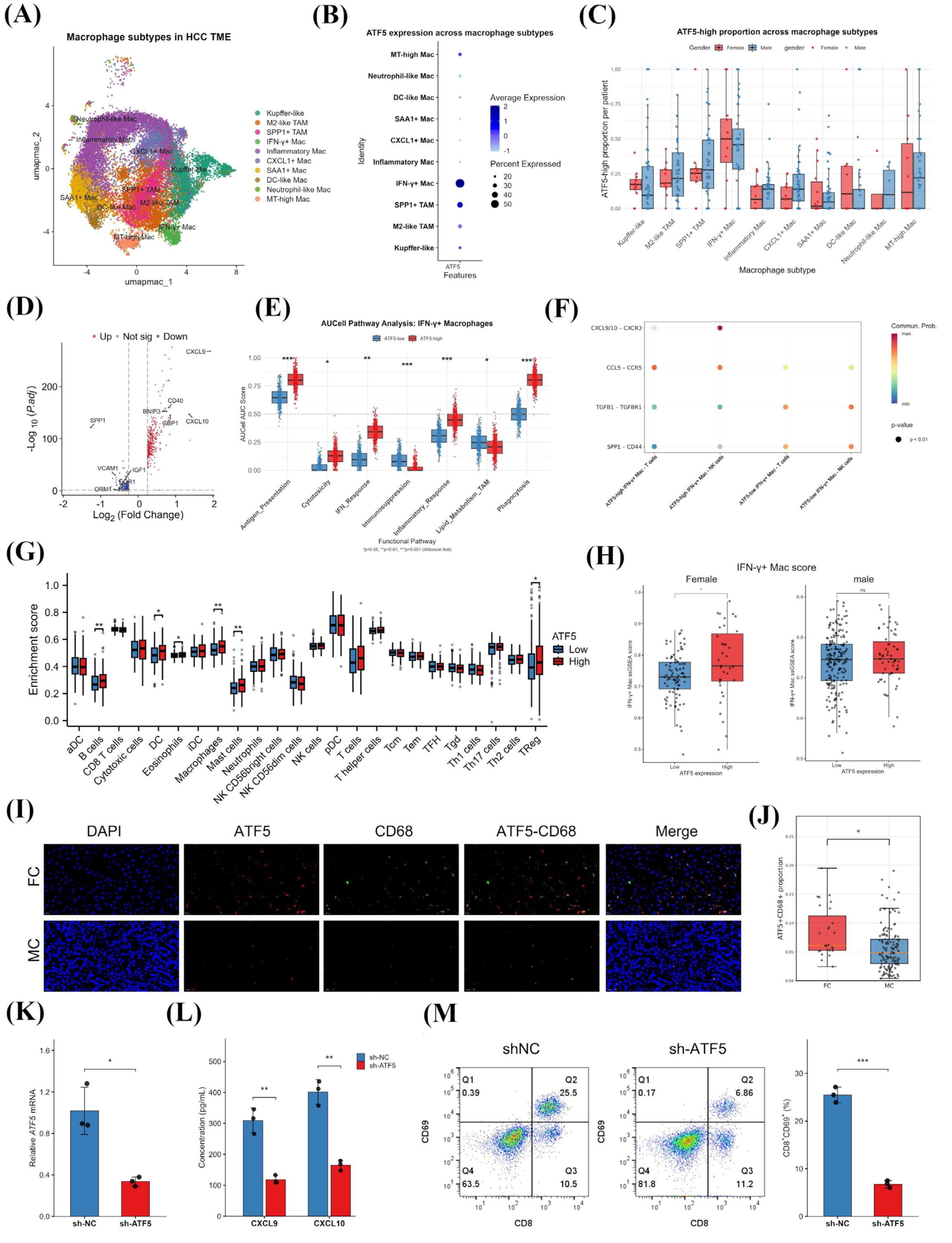

Figure 3. ATF5 delineates a female-enriched tumor-associated macrophage (TAM) state with enhanced immunostimulatory programs and CD8/NK communication. (A) UMAP of macrophage subclusters and subtype annotation; interferon-γ (IFN-γ)$^+$ macrophages are defined by interferon-stimulated gene expression. **(B)** ATF5 expression across macrophage subtypes (dot plot). **(C)** Sex-stratified proportion of ATF5-high macrophages within subtypes (definition indicated in the panel). **(D)** Differential expression between ATF5-high and ATF5-low IFN-γ$^+$ macrophages (volcano plot; thresholds indicated in the panel). **(E)** AUCell module scores comparing ATF5-high versus ATF5-low IFN-γ$^+$ macrophages (modules and significance indicated in the panel). **(F)** CellChat ligand–receptor communication from IFN-γ$^+$ macrophages to CD8 T and natural killer (NK) cells; representative interactions are highlighted. **(G)** TCGA-LIHC bulk immune infiltration estimated by single-sample gene set enrichment analysis (ssGSEA) stratified by ATF5 expression. **(H)** IFN-γ$^+$ macrophage signature score (ssGSEA) stratified by ATF5 and sex. **(I)** Representative mIF images of ATF5 and CD68 in FC *vs*. MC tumors (scale bar shown). **(J)** Quantification of ATF5$^+$CD68$^+$ cells (summary statistic and test indicated in the panel). **(K)** qPCR validation of ATF5 knockdown efficiency in PMA-differentiated THP-1 macrophages. **(L)** ELISA quantification of CXCL9 and CXCL10 in conditioned medium from sh-NC and shATF5 macrophages. **(M)** Representative flow cytometry dot plots (left) and quantification (right) of CD8$^+$CD69$^+$ T cells after co-culture with conditioned medium from sh-NC or shATF5 macrophages.

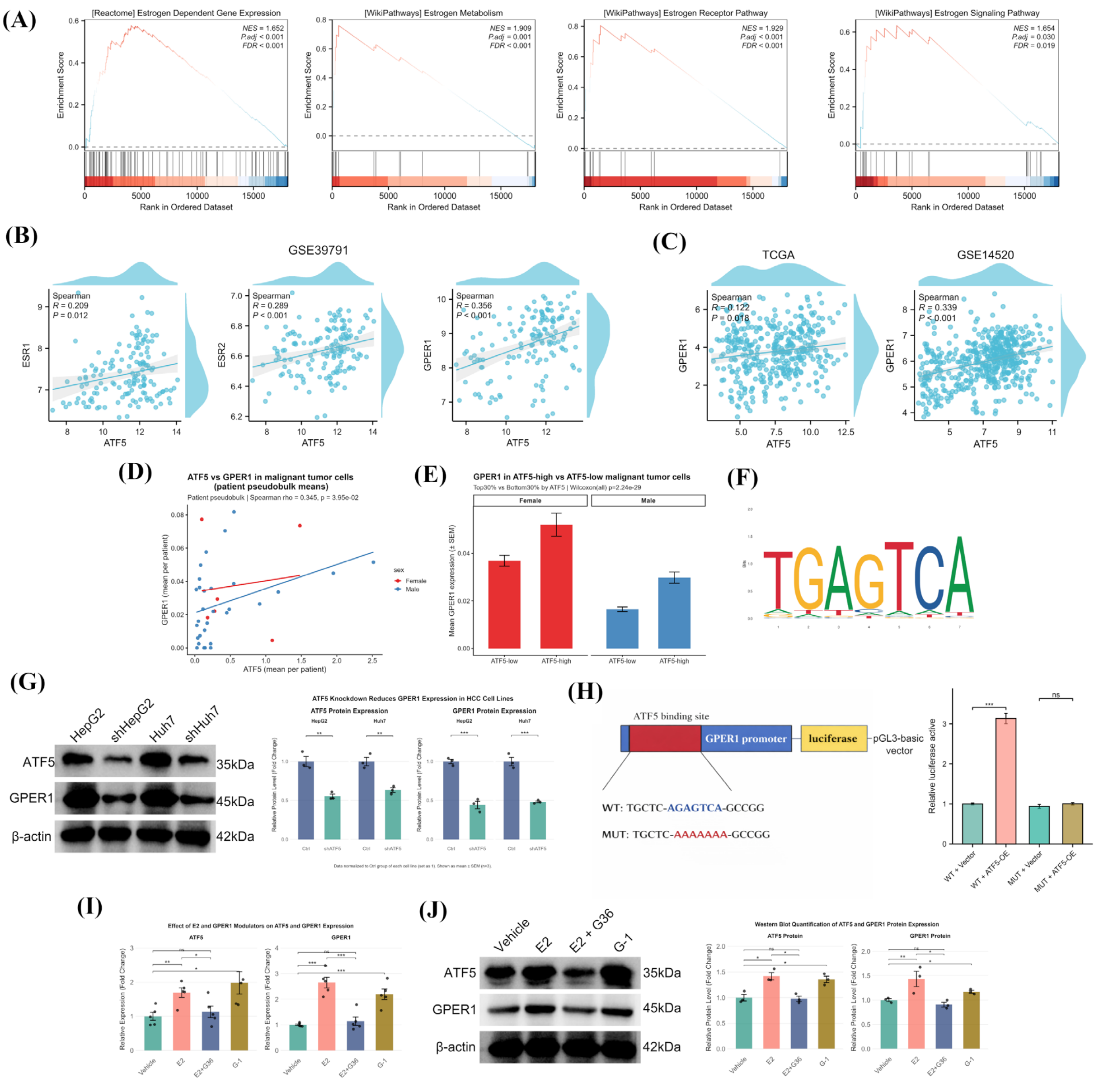

Figure 4. ATF5 transcriptionally activates GPER1 and responds to estrogen signaling. (A) Gene set enrichment analysis (GSEA) showing enrichment of estrogen-related pathways in ATF5-high versus ATF5-low tumors (GSE39791). **(B)** Correlation of ATF5 with estrogen receptor genes (ESR1/ESR2) and G protein–coupled estrogen receptor 1 (GPER1) in GSE39791 (Spearman ρ and *p* shown). **(C)** Validation of ATF5–GPER1 correlation in independent bulk cohorts (TCGA-LIHC and GSE14520). **(D)** Patient-level pseudobulk correlation of ATF5 and GPER1 in malignant cells from the scRNA-seq atlas. **(E)** GPER1 expression in malignant cells stratified by ATF5 (ATF5-high vs ATF5-low), with sex stratification. **(F)** ATF5 motif logo from the JASPAR database. **(G)** Western blot showing short hairpin RNA (shRNA)-mediated ATF5 knockdown reduces GPER1 in HepG2 and Huh7 (quantification shown). **(H)** Dual-luciferase assay using wild-type and motif-mutant (WT/MUT) GPER1 promoter reporters demonstrating ATF5-dependent transactivation. **(I)** Quantitative real-time PCR (qRT-PCR) of ATF5 and GPER1 following hormone/GPER1-modulator treatments (Vehicle, 17β-estradiol [E2], G-1, and E2+G36). **(J)** Western blot validation under the same treatment conditions.

fold, $p < 0.01$; Figure 4J).

To explore the mechanistic basis of female-biased ATF5 expression, we examined whether the ATF5 promoter contains EREs or exhibits sex-differential DNA methylation. FIMO analysis identified no classical ESR1-binding EREs (JASPAR MA0112.3, $p < 1\times10^{-4}$), but revealed three putative ERβ binding sites (JASPAR MA0258.1, $p < 0.001$), with ESR2 Site 1 located only 24 bp from CpG probe cg00423055 (Supplementary Figure S4A, *https://www.biosciencetrends.com/action/getSupplementalData.php?ID=290*). DNA methylation at all four ATF5 promoter CpG probes showed no significant sex difference in either tumor or normal tissue (all $p > 0.05$; Supplementary Figure S4B, S4C, *https://www.biosciencetrends.com/action/getSupplementalData.php?ID=290*), and promoter methylation did not correlate significantly with ATF5 expression in tumor tissue (Spearman r = −0.097, $p = 0.061$; Supplementary

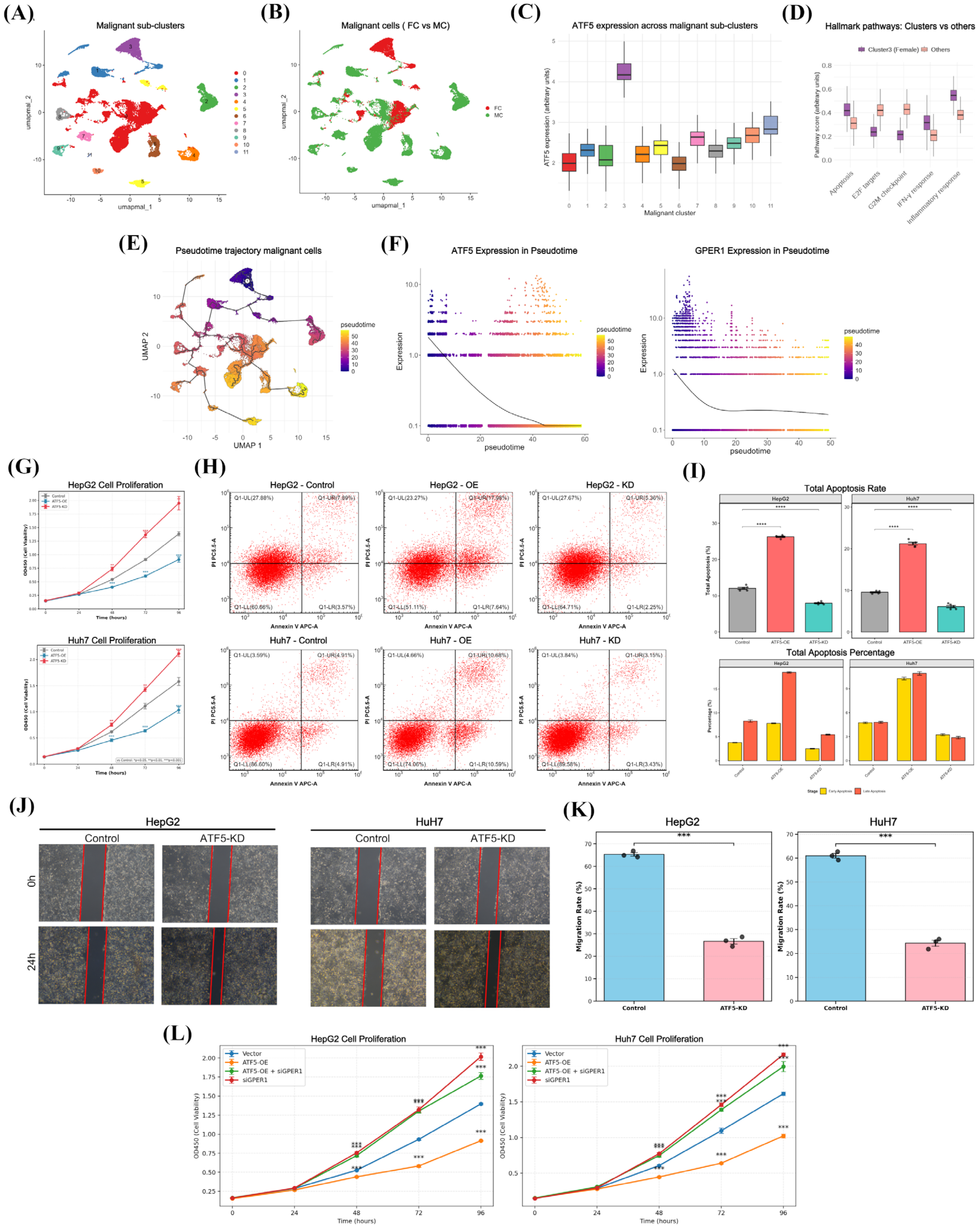

Figure 5. ATF5 defines a female-enriched malignant subcluster and suppresses HCC progression *via* GPER1-dependent mechanisms. (A) UMAP of inferCNV-defined malignant cells re-clustered into malignant subclusters. **(B)** UMAP colored by sex, highlighting a female-enriched malignant subcluster. **(C)** ATF5 expression across malignant subclusters (box plots; comparison indicated in the panel). **(D)** Hallmark pathway activity (AUCell) comparing the female-enriched subcluster versus other malignant cells. **(E)** Monocle3 pseudotime trajectory of malignant cells (root indicated in the panel). **(F)** ATF5 and GPER1 expression dynamics along pseudotime. **(G)** Cell Counting Kit-8 (CCK-8) proliferation assays following ATF5 overexpression (OE) or knockdown (KD) in HepG2 and Huh7. **(H)** Representative flow cytometry plots for apoptosis measured by Annexin V/7-AAD staining. **(I)** Quantification of apoptosis across conditions (tests indicated in the panel). **(J)** Representative wound-healing images at 0 h and 24 h. **(K)** Quantification of migration/wound closure (tests indicated in the panel). **(L)** GPER1 rescue experiment showing reversal of ATF5-mediated growth suppression by small interfering RNA (siRNA)-mediated GPER1 knockdown.

Figure S4D, *https://www.biosciencetrends.com/action/getSupplementalData.php?ID=290*). These results indicate that promoter hypomethylation does not drive female-biased ATF5 expression, and suggest that estrogen regulates ATF5 preferentially through non-classical ERβ/GPER signaling, consistent with the ATF5 upregulation observed following G-1 treatment.

3.5. ATF5 defines a low-grade malignant subcluster and suppresses tumor progression *via* GPER1-dependent mechanisms

Malignant cell reclustering (n = 38,844, resolution 0.8) identified 12 subclusters, with Cluster 3 being female-enriched and exhibiting highest ATF5 expression (median 0.476 *vs*. others 0.15–0.35; Wilcoxon $p < 0.001$; Figure 5A-C). Hallmark pathway enrichment revealed Cluster 3 elevated in Apoptosis (median AUC 0.448 *vs*. 0.321; FDR = 0.008), Inflammatory response (0.572 *vs*. 0.381; FDR < 0.001), and IFN-γ response (0.351 *vs*. 0.224; FDR = 0.042), but reduced in E2F targets (0.253 *vs*. 0.428; FDR < 0.001) and G2M checkpoint (0.218 *vs*. 0.451; FDR < 0.001; Figure 5D).

Pseudotime trajectory analysis using Monocle3 positioned Cluster 3 at the origin (pseudotime 0), with coordinated downregulation of ATF5 (mean expression: pseudotime 0 = 0.51 to pseudotime 60 = 0.09; Spearman $\rho = -0.52$, $p < 0.001$) and GPER1 ($\rho = -0.48$, $p < 0.001$) during malignant progression (Figure 5E-F).

Functional validation showed ATF5 overexpression (ATF5-OE) suppressed proliferation at 96 hours (HepG2: OD_{450} 0.911 ± 0.107 *vs*. Control 1.383 ± 0.086, $p < 0.001$; Huh7: 1.036 ± 0.136 *vs*. 1.581 ± 0.168, $p < 0.001$), while ATF5 knockdown (ATF5-KD) enhanced growth (HepG2: 1.949 ± 0.277; Huh7: 2.017 ± 0.126; both $p < 0.001$; Figure 5G). Flow cytometric analysis using Annexin V-APC/7-AAD demonstrated ATF5-OE markedly increased total apoptosis (HepG2: 26.45 ± 0.35% *vs*. Control 11.88 ± 0.87%, $p < 0.0001$; Huh7: 21.20 ± 0.75% *vs*. 9.49 ± 0.27%, $p < 0.0001$), including both early and late apoptotic populations, whereas ATF5-KD reduced apoptosis (HepG2: 7.95 ± 0.61%; Huh7: 6.14 ± 0.57%; both $p < 0.001$; Figure 5H-I). Wound-healing assays demonstrated ATF5-KD enhanced migration at 24 hours (HepG2: 26.61% remaining wound area *vs*. Control 65.31%, $p < 0.001$; Huh7: 24.29% *vs*. 60.99%, $p < 0.001$; Figure 5J-K).

GPER1 rescue experiments demonstrated that siRNA-mediated GPER1 knockdown (siGPER1) reversed ATF5-OE-mediated growth suppression at 96 hours (HepG2: ATF5-OE 0.914 ± 0.016 *vs*. Vector 1.397 ± 0.027, $p < 0.001$; ATF5-OE + siGPER1 1.764 ± 0.100, $p < 0.001$ *vs*. ATF5-OE alone; Huh7: ATF5-OE 1.023 ± 0.060 *vs*. Vector 1.614 ± 0.056, $p < 0.001$; ATF5-OE + siGPER1 1.996 ± 0.155, $p < 0.001$ *vs*. ATF5-OE alone; Figure 5L), establishing GPER1 as functionally required for ATF5-mediated tumor suppression.

4. Discussion

This study identifies the ATF5-GPER1 axis as a female-protective molecular circuit in hepatocellular carcinoma operating through integrated tumor-suppressive and immune-modulatory mechanisms. Our tissue-specific demonstration of ATF5's tumor-suppressive function in liver cancer contrasts with its oncogenic roles in other malignancies (*17*), —most notably in glioblastoma, where ATF5 sustains tumor cell survival through BCL-2 and MCL-1 upregulation and is actively pursued as a therapeutic target *via* dominant-negative peptides (*19,20*); in breast cancer, where ATF5 loss of function selectively induces apoptosis in malignant but not normal mammary cells (*19*); and in lung adenocarcinoma, where ATF5 promotes radioresistance and malignant regrowth through cell cycle acceleration (*21*). This striking context-dependency—oncogenic in neural, mammary, and pulmonary tumors yet tumor-suppressive in hepatocytes—likely reflecting differential cofactor availability and chromatin landscapes across tissues—a phenomenon observed with other transcription factors such as PPARγ (*22*). In hepatocytes specifically, the abundant availability of ATF/CREB family co-activators and the liver-enriched chromatin architecture may redirect ATF5 transcriptional output toward pro-apoptotic and stress-response gene programs rather than the survival circuits it activates in glioma. This interpretation is consistent with the tissue-restricted expression patterns of ATF5's known co-repressors and with our observation that ATF5 overexpression in hepatocellular lines drives apoptosis and growth arrest rather than the resistance phenotypes described in neural tumor models (*19,20*). Understanding this switch in transcriptional polarity will be essential before any therapeutic strategy targeting ATF5 can be considered across cancer types. Critically, ATF5's protective effects are mediated through direct GPER1 transactivation, establishing a non-canonical estrogen signaling pathway that reconciles the long-standing paradox of why classical ERα-targeted therapies have failed clinically despite strong epidemiologic evidence for female survival advantage (*23,24*). This finding suggests that therapeutic strategies should pivot toward GPER1-selective agonists or interventions enhancing ATF5 expression rather than continuing to target classical nuclear estrogen receptors.

A central innovation of our study lies in applying single-cell transcriptomics to systematically dissect sex differences in HCC at cellular resolution—an approach that has revealed sex-biased tumor cell states in lung cancer and melanoma but remained underutilized in HCC (*14,25*). Through inferCNV-based malignant cell identification and pseudotime analysis, we discovered that ATF5 marks a female-enriched, transcriptionally distinct malignant subcluster positioned at the origin of tumor progression trajectories. The coordinated downregulation of ATF5 and GPER1 during malignant evolution (Spearman $\rho = -0.52$ and -0.48) suggests that loss of this axis may represent a critical evolutionary bottleneck in HCC development, particularly relevant for female patients who initially benefit from higher ATF5 expression. This extends beyond previous sex-dimorphism studies that focused predominantly on hormone receptors or chromosomal factors by identifying a transcription factor whose sex-biased expression arises from complex hormonal and microenvironmental regulation (*26*).

Our macrophage-focused analyses revealed an unexpected role for ATF5 in shaping tumor immunity. The identification of a female-enriched IFN-γ^+ macrophage subset marked by high ATF5 expression provides mechanistic insight into how sex-specific gene expression translates to differential immune infiltration patterns—a phenomenon widely observed but poorly understood mechanistically (*9,27*). The preferential engagement of CD8$^+$ T cells and NK cells through CXCL9/10–CXCR3 and CCL5 signaling by ATF5-high macrophages, contrasted with immunosuppressive TGFB and SPP1 interactions in ATF5-low cells, suggests that ATF5 status may predict immunotherapy responsiveness. This hypothesis aligns with emerging evidence that female cancer patients show more durable benefit from immune checkpoint inhibitors despite lower initial response rates and warrants prospective validation in clinical trials stratifying patients by ATF5 expression (*10,28*).

The mechanistic demonstration that ATF5 directly transactivates GPER1 through consensus motif binding, coupled with functional rescue experiments showing GPER1 dependence, establishes a regulatory hierarchy absent from prior literature. GPER1 has emerged as a mediator of rapid non-genomic estrogen signaling distinct from classical nuclear ER pathways (*29,30*), with protective effects demonstrated in cardiovascular and nervous systems (*31*). However, its role in HCC has remained controversial (*32*), likely due to overlooking the requirement for ATF5-mediated transcriptional activation. Our hormone modulation experiments showing coordinated upregulation of both ATF5 and GPER1 by estradiol and G-1, with G36 antagonist abrogating these effects, establish a positive feedback loop that amplifies estrogen-responsive protection specifically in females with elevated endogenous ATF5. This context-dependency explains previous inconsistencies and underscores the importance of considering transcriptional regulation and hormonal milieu when evaluating GPER1's function.

From a precision oncology perspective, several translational opportunities emerge. First, ATF5 expression could stratify patients for immunotherapy trials, as ATF5-high tumors exhibit immunostimulatory macrophage enrichment and enhanced chemokine-mediated lymphocyte recruitment—features associated with checkpoint inhibitor responsiveness (*33,34*). Second, the sex-specific prognostic value of ATF5 (HR = 0.34 in females, $p = 0.040$ *vs.* HR = 0.69 in males, P=0.080) supports developing sex-stratified risk calculators incorporating ATF5 status alongside established clinical variables, moving beyond one-size-fits-all prognostic models. Third, female patients with low ATF5 expression represent a high-risk subgroup lacking protective benefit who may warrant more aggressive surveillance or adjuvant therapy, whereas ATF5-high females with early-

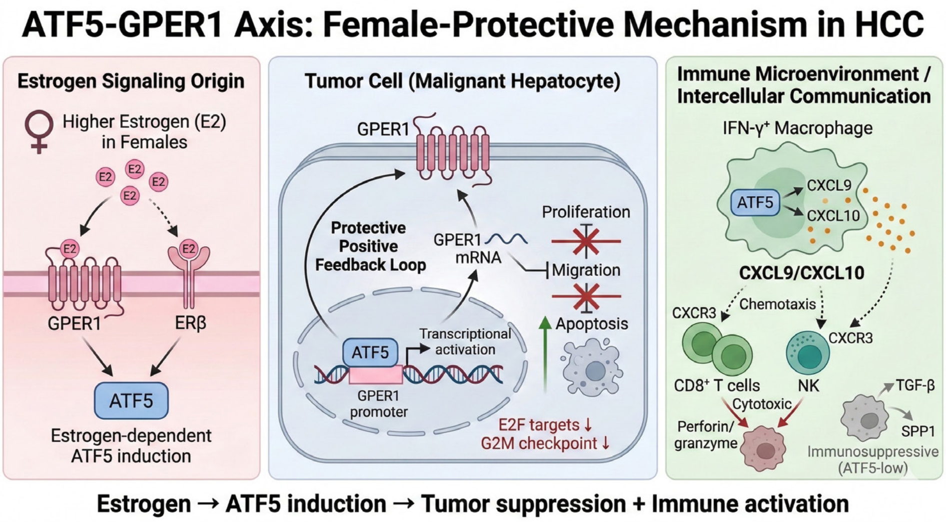

Figure 6. Schematic model of the ATF5–GPER1 axis as a female-protective mechanism in hepatocellular carcinoma. In females, higher circulating estrogen (E2) activates ATF5 through GPER1 (solid arrow) and ERβ (dashed arrow) signaling. Within malignant hepatocytes, ATF5 transcriptionally activates the GPER1 promoter, forming a protective positive feedback loop that suppresses proliferation and migration while promoting apoptosis, with concurrent downregulation of E2F targets and G2M checkpoint pathways. In IFN-γ^+ macrophages, ATF5 drives secretion of CXCL9 and CXCL10, which recruit cytotoxic CD8$^+$ T cells and NK cells to the tumor microenvironment *via* the CXCR3 axis. In contrast, ATF5-low macrophages exhibit immunosuppressive phenotypes characterized by TGF-β and SPP1 signaling.

stage disease could benefit from less intensive follow-up.

Several limitations warrant consideration. Our immune findings are primarily correlative from single-cell data; definitive causality requires macrophage-specific ATF5 manipulation in appropriate preclinical models. The modest TMA cohort size (*n* = 167) and single-center derivation limit generalizability, necessitating multi-center validation across diverse etiologies (HBV, HCV, NASH, alcohol-related) and geographic populations. The incomplete characterization of ATF5's complete transcriptional program beyond GPER1, and undefined mechanisms underlying ATF5's sex-biased expression (epigenetic regulation, microRNA control), represent areas for future investigation. Additionally, whether therapeutic modulation of the ATF5-GPER1 axis through GPER1 agonists or ATF5-enhancing interventions can recapitulate naturally occurring protection requires extensive preclinical optimization and safety evaluation.

In conclusion, our study establishes ATF5-GPER1 as a female-protective axis in hepatocellular carcinoma, linking tumor suppression with an immunostimulatory macrophage program (Figure 6). By demonstrating direct ATF5-dependent GPER1 transactivation, we define a non-canonical estrogen pathway that reconciles the clinical failure of ERα-directed approaches with consistent female survival advantage. Targeting this axis—through GPER1-selective agonists or interventions boosting ATF5—may offer a rational sex-informed therapeutic strategy.

Funding: This study was funded by the National Natural Science Foundation of China (No. 82170666 and 82572988), and Chongqing science and health joint project (2024GGXM005).

Conflict of Interest: The authors have no conflicts of interest to disclose.

Ethical statement: This study was reviewed and approved by the Ethics Committee of the First Affiliated Hospital of Chongqing Medical University (Approval No. 2024-607-01) and received institutional scientific review approval (Approval No. KX2024-KYC0273-01).

Availability of data and materials: All original data can be available from the corresponding authors based on the reasonable request.

References

1. Bray F, Laversanne M, Sung H, Ferlay J, Siegel RL, Soerjomataram I, Jemal A. Global cancer statistics 2022: GLOBOCAN estimates of incidence and mortality worldwide for 36 cancers in 185 countries. CA Cancer J Clin. 2024; 74:229-263.
2. Burra P, Bizzaro D, Gonta A, Shalaby S, Gambato M, Morelli MC, Trapani S, Floreani A, Marra F, Brunetto MR, Taliani G, Villa E. Clinical impact of sexual dimorphism in non-alcoholic fatty liver disease (NAFLD) and non-alcoholic steatohepatitis (NASH). Liver Int. 2021; 41:1713-1733.
3. Xu ZQ, Luo SQ, Wu ZJ, Liao R. Current status and perspectives of molecular mechanisms of gender difference in hepatocellular carcinoma: The tip of the iceberg? Biosci Trends. 2025; 19:266-280.
4. Haupt S, Caramia F, Klein SL, Rubin JB, Haupt Y. Sex disparities matter in cancer development and therapy. Nat Rev Cancer. 2021; 21:393-407.
5. Ruggieri A, Gagliardi MC, Anticoli S. Sex-Dependent Outcome of Hepatitis B and C Viruses Infections: Synergy of Sex Hormones and Immune Responses? Front Immunol. 2018; 9:2302.
6. Shi L, Feng Y, Lin H, Ma R, Cai X. Role of estrogen in hepatocellular carcinoma: is inflammation the key? J Transl Med. 2014; 12:93.
7. Llovet JM, Montal R, Sia D, Finn RS. Molecular therapies and precision medicine for hepatocellular carcinoma. Nat Rev Clin Oncol. 2018; 15:599-616.
8. Pfister D, Núñez NG, Pinyol R, *et al*. NASH limits anti-tumour surveillance in immunotherapy-treated HCC. Nature. 2021; 592:450-456.
9. Shen KY, Zhu Y, Xie SZ, Qin LX. Immunosuppressive tumor microenvironment and immunotherapy of hepatocellular carcinoma: current status and prospectives. J Hematol Oncol. 2024; 17:25.
10. Wallis CJD, Butaney M, Satkunasivam R, Freedland SJ, Patel SP, Hamid O, Pal SK, Klaassen Z. Association of Patient Sex With Efficacy of Immune Checkpoint Inhibitors and Overall Survival in Advanced Cancers: A Systematic Review and Meta-analysis. JAMA Oncol. 2019; 5:529-536.
11. Qian J, Olbrecht S, Boeckx B, *et al*. A pan-cancer blueprint of the heterogeneous tumor microenvironment revealed by single-cell profiling. Cell Res 2020; 30:745-762.
12. Yu Y, You Y, Duan Y, *et al*. Multi-omics approaches for identifying the PANoptosis signature and prognostic model *via* a multimachine-learning computational framework for intrahepatic cholangiocarcinoma. Hepatology. 2026; 83:466-483.
13. Laughney AM, Hu J, Campbell NR, *et al*. Regenerative lineages and immune-mediated pruning in lung cancer metastasis. Nat Med. 2020; 26:259-269.
14. Jerby-Arnon L, Shah P, Cuoco MS, *et al*. A Cancer Cell Program Promotes T Cell Exclusion and Resistance to Checkpoint Blockade. Cell. 2018; 175:984-997.e924.
15. Chen Z, Zhou L, Liu L, Hou Y, Xiong M, Yang Y, Hu J, Chen K. Single-cell RNA sequencing highlights the role of inflammatory cancer-associated fibroblasts in bladder urothelial carcinoma. Nat Commun. 2020; 11:5077.
16. Ishihara S, Enomoto A, Sakai A, Iida T, Tange S, Kioka N, Nukuda A, Nagasato AI, Yasuda M, Tokino T, Haga H. Stiff extracellular matrix activates the transcription factor ATF5 to promote the proliferation of cancer cells. iScience. 2025; 28:112057.
17. Sheng Z, Li L, Zhu LJ, Smith TW, Demers A, Ross AH, Moser RP, Green MR. A genome-wide RNA interference screen reveals an essential CREB3L2-ATF5-MCL1 survival pathway in malignant glioma with therapeutic implications. Nat Med. 2010; 16:671-677.
18. Barton M, Filardo EJ, Lolait SJ, Thomas P, Maggiolini M, Prossnitz ER. Twenty years of the G protein-coupled

estrogen receptor GPER: Historical and personal perspectives. J Steroid Biochem Mol Biol. 2018; 176:4-15.

19. Dluzen D, Li G, Tacelosky D, Moreau M, Liu DX. BCL-2 is a downstream target of ATF5 that mediates the prosurvival function of ATF5 in a cell type-dependent manner. J Biol Chem. 2011; 286:7705-7713.
20. Cates CC, Arias AD, Nakayama Wong LS, Lamé MW, Sidorov M, Cayanan G, Rowland DJ, Fung J, Karpel-Massler G, Siegelin MD, Greene LA, Angelastro JM. Regression/eradication of gliomas in mice by a systemically-deliverable ATF5 dominant-negative peptide. Oncotarget. 2016; 7:12718-12730.
21. Ishihara S, Yasuda M, Ishizu A, Ishikawa M, Shirato H, Haga H. Activating transcription factor 5 enhances radioresistance and malignancy in cancer cells. Oncotarget. 2015; 6:4602-4614.
22. Yoshimura R, Matsuyama M, Segawa Y, Hase T, Mitsuhashi M, Tsuchida K, Wada S, Kawahito Y, Sano H, Nakatani T. Expression of peroxisome proliferator-activated receptors (PPARs) in human urinary bladder carcinoma and growth inhibition by its agonists.Int J Cancer. 2003; 104:597-602.
23. Naing C, Ni H, Aung HH. Tamoxifen for adults with hepatocellular carcinoma. Cochrane Database Syst Rev. 2024; 8:Cd014869.
24. Zhang L, Wu J, Wu Q, Zhang X, Lin S, Ran W, Zhu L, Tang C, Wang X. Sex steroid axes in determining male predominance in hepatocellular carcinoma. Cancer Lett. 2023; 555:216037.
25. Kim N, Kim HK, Lee K, *et al*. Single-cell RNA sequencing demonstrates the molecular and cellular reprogramming of metastatic lung adenocarcinoma. Nat Commun. 2020; 11:2285.
26. Kur P, Kolasa-Wołosiuk A, Misiakiewicz-Has K, Wiszniewska B. Sex Hormone-Dependent Physiology and Diseases of Liver. Int J Environ Res Public Health. 2020; 17.
27. Jacobsen H, Klein SL. Sex Differences in Immunity to Viral Infections. Front Immunol. 2021; 12:720952.
28. Vacher L, Bernadach M, Molnar I, Passildas-Jahanmohan J, Dubray-Longeras P. The efficacy of immune checkpoint inhibitors following discontinuation for long-term response or toxicity in advanced or metastatic non-small-cell lung cancers: A retrospective study. Health Sci Rep. 2024; 7:e1825.
29. Tang X, Liao Q, Li Q, Jiang L, Li W, Xu J, Xiong A, Wang R, Zhao J, Wang Z, Ding L, Yang L. Lusianthridin ameliorates high fat diet-induced metabolic dysfunction-associated fatty liver disease *via* activation of FXR signaling pathway. Eur J Pharmacol. 2024; 965:176196.
30. Xu S, Yu S, Dong D, Lee LTO. G Protein-Coupled Estrogen Receptor: A Potential Therapeutic Target in Cancer. Front Endocrinol (Lausanne). 2019; 10:725.
31. Dinh QN, Vinh A, Arumugam TV, Drummond GR, Sobey CG. G protein-coupled estrogen receptor 1: a novel target to treat cardiovascular disease in a sex-specific manner? Br J Pharmacol. 2021; 178:3849-3863.
32. Chaturantabut S, Shwartz A, Evason KJ, *et al.* Estrogen Activation of G-Protein-Coupled Estrogen Receptor 1 Regulates Phosphoinositide 3-Kinase and mTOR Signaling to Promote Liver Growth in Zebrafish and Proliferation of Human Hepatocytes. Gastroenterology. 2019; 156:1788-1804.e1713.
33. Llovet JM, Pinyol R, Kelley RK, El-Khoueiry A, Reeves HL, Wang XW, Gores GJ, Villanueva A. Molecular pathogenesis and systemic therapies for hepatocellular carcinoma. Nat Cancer. 2022; 3:386-401.
34. Wu K. Research highlights of clinical oncology early 2022. Holist Integr Oncol. 2022; 1:6.

Received January 28, 2026; Revised March 6, 2026; Accepted March 14, 2026.

[§] These authors contributed equally to this work.

**Address correspondence to:*
Zhongjun Wu and Rui Liao, Department of Hepatobiliary Surgery, the First Affiliated Hospital of Chongqing Medical University, 1 Youyi Road, Yuzhong District, Chongqing 400016, China.
E-mail: wzjtcy@126.com (ZW); liaorui99@163.com (RL)